



Cite this: *Soft Matter*, 2019,  
15, 6288

## Computational self-assembly of colloidal crystals from Platonic polyhedral sphere clusters<sup>†</sup>

Ryan L. Marson, <sup>ab</sup> Erin G. Teich, <sup>c</sup> Julia Dshemuchadse, <sup>ab</sup> Sharon C. Glotzer <sup>abcd</sup> and Ronald G. Larson\*<sup>ab</sup>

We explore a rich phase space of crystals self-assembled from colloidal “polyhedral sphere clusters (PSCs),” each of which consists of equal-sized “halo” spheres placed at the vertices of a polyhedron such that they just touch along each edge. Such clusters, created experimentally by fusing spheres, can facilitate assembly of useful colloidal crystal symmetries not attainable by unclustered spheres. While not crucial for their self-assembly, the center of the PSC can contain a “core” particle that can be used as a scaffold to build the PSC. Using Brownian dynamics simulations, we show the self-assembly of eight distinct crystalline phases from PSCs that correspond to the five Platonic polyhedra, and that are made of spheres with purely repulsive interactions. Strong crystalline order is seen in the centers of mass of the PSCs, or equivalently the core particles. The halo particles also may organize into crystal structures, usually with weaker crystalline order than the core particles. Notably, however, in crystals assembled from the octahedral and icosahedral PSCs, the halo particles are also well ordered, nesting within the crystals formed by the cores. Interestingly, despite the rounded nature of the PSCs, in some cases we obtain structures similar to those of the corresponding faceted polyhedra interacting only via excluded volume. Only the tetrahedral PSCs fail to self-assemble into a crystal, but we demonstrate that a pre-assembled crystal – whose halo particles sit on a close-packed face-centered cubic lattice, and whose core particles form a diamond structure – is stable at high density and melts into a hexagonal phase at lower density.

Received 1st April 2019,  
Accepted 3rd July 2019

DOI: 10.1039/c9sm00664h

[rsc.li/soft-matter-journal](http://rsc.li/soft-matter-journal)

### 1 Introduction

Colloids, ubiquitous in day-to-day life in products ranging from food to shampoo to textiles, are also of interest for many experimental applications. They provide optically visible analogs for atomic or molecular structures, and readily crystallize into a variety of ordered structures that depend on particle shape, size, and charge.<sup>1–6</sup> With careful design, colloidal crystals can possess unusual but technologically promising properties such as structural color,<sup>7</sup> which arises from the packings of constituent colloidal particles rather than from molecular dyes. Structural color, as is present for example in the wings of some butterfly species<sup>8–10</sup> is vivid and bright, and does not fade with time. Perhaps most importantly, next-generation computers that use light rather than electrons to operate orders of magnitude faster than current devices may be able to leverage the precisely defined spacings in colloidal

crystal structures<sup>3</sup> to conduct photons in a wavelength-dependent manner (analogous to similar selective conduction of electrons in atomic crystals).<sup>11,12</sup> Of particular technological interest is the diamond family of structures, long sought for its photonic properties.<sup>11–18</sup>

The pursuit of these photonic and related technologies requires that researchers spatially order colloidal particles in a controlled, cost-effective, reproducible manner.<sup>2–4,19</sup> Attempts to do so began simply, with micron-sized monodisperse polymer spheres that were densified in various ways including evaporation<sup>20</sup> and microfluidic techniques.<sup>21,22</sup> Ultimately, most of these experiments resulted in the crystallization of the FCC structure,<sup>2–4</sup> which is the densest packing of monodisperse hard spheres.<sup>23</sup> To obtain different structures, researchers have sought ways to introduce anisotropy into the interactions of these colloids, as it is now well-understood that anisotropic interactions, mediated for example by colloidal shape or patterning, can lead to new equilibrium morphologies.<sup>1,5</sup> This understanding has led to a new wave of various synthesis techniques, chief among them the assembly of building blocks using droplet evaporation,<sup>24,25</sup> DNA ligand-capped anisotropic nanoparticle synthesis,<sup>26</sup> and the use of colloid-tethered DNA as a specific<sup>17,20,25,27–29</sup> or directional<sup>30,31</sup> binding agent.<sup>22,32</sup> Such building blocks are then used to assemble a variety

<sup>a</sup> Department of Chemical Engineering, University of Michigan, Ann Arbor, MI 48109, USA. E-mail: [rlarson@umich.edu](mailto:rlarson@umich.edu)

<sup>b</sup> Biointerfaces Institute, University of Michigan, Ann Arbor, MI 48109, USA

<sup>c</sup> Applied Physics Program, University of Michigan, Ann Arbor, MI 48109, USA

<sup>d</sup> Department of Materials Science and Engineering, University of Michigan, Ann Arbor, MI 48109, USA

<sup>†</sup> Electronic supplementary information (ESI) available. See DOI: [10.1039/c9sm00664h](https://doi.org/10.1039/c9sm00664h)

of single-component and binary crystal structures.<sup>15,17,28,29,33–38</sup> Other methods for assembly that rely on shape and entropy are particularly appealing due to the simplicity of the assembly process, which requires no interactions other than excluded volume among the particles,<sup>1,39–42</sup> and can be achieved merely by crowding the particles. Hard polyhedra, for example, assemble into a host of diverse crystal structures,<sup>40,41,43</sup> some of which have been experimentally realized.<sup>43,44</sup> Recently, McGinley *et al.*<sup>30,45</sup> put forth a method of synthesizing purely repulsive anisotropic colloids by exploiting a “core”–“halo” packing of spheres to create polyhedral clusters such as tetrahedra, octahedra, and icosahedra. Here we investigate *via* molecular simulation the self-assembly of rigid, pre-formed core–halo polyhedral sphere clusters (PSCs) to explore the range of crystal structures that can be formed from rigid clusters of purely repulsive hard spheres.

We define a PSC as a sphere cluster for which the set of all bonds connecting the centers of tangent spheres forms a polyhedron. In our definition, we require all spheres of a PSC to be tangent spheres (that is, no overlap is permitted within a PSC). This definition of PSCs intentionally excludes clusters for which there are bonds that are not part of a polygon forming the face of a polyhedron – for example, a tetrahedral cluster with a fifth sphere attached solely to one corner of the tetrahedron. We further define a “regular” PSC as one in which all spheres are the same size. Any polyhedron whose edges are all the same length can therefore frame a regular PSC. If the edges of the polyhedron are not all the same length, then equi-sized spheres cannot touch along each edge of that polyhedron. Hence only polyhedra with the same edge lengths can be scaffolds for regular PSCs. Thus, one can construct “Archimedean PSCs”, “Catalan PSCs” (duals of the Archimedean PSCs), and “Johnson PSCs”, along with the “Platonic PSCs”, all of which are regular because they all have edges of equal length.

We also define a general class of “halo sphere clusters” (HSCs), with a central sphere core surrounded by a layer of halo spheres, all of which touch the central sphere. In a regular HSC, all halo spheres are the same size but possibly different from the size of the core sphere. This type of cluster has already been defined previously.<sup>46,47</sup> For some HSCs the halo spheres form PSCs; but, in general, the regular PSCs are a subset of HSCs. Beyond this, one can define “multilayer” HSCs with second, third, or more layers of halo spheres, where the  $n$ th order halo spheres must all touch one or more of the  $(n - 1)$ th layer spheres.

Because the vertices of Platonic and Archimedean solids are all equivalent, for each of these, there exists a regular core–halo cluster. That is, the touching spheres at the vertices of the Platonic or Archimedean PSCs all can also touch a central core sphere of appropriately-chosen size. The Catalan and Johnson polyhedra do not universally possess this property because, although the edges of a Catalan or Johnson polyhedron are all the same length, not all vertices are equivalent; thus, a central sphere can touch some vertex spheres without touching them all. The ability of the central sphere to touch all halo spheres is important not only for determining the symmetries of the self-assembled phases, but also for synthesizing these sphere clusters by binding halo spheres to the central spheres. It should be noted

that while the arrangements of the core particles are discussed in our study (due to their use as scaffolds onto which the halo particles of the PSC are frequently assembled experimentally), they play no direct role in the self-assembly of the PSC clusters into crystalline phases, because their short-range (contact) interactions do not reach beyond the surrounding halo particles in which each core particle is buried. We refer to these colloidal clusters as PSCs because the halo particles alone drive their crystalline self-assembly. PSCs could be synthesized without a core particle as a scaffold, for example by shrinking a droplet containing the desired number of equal-sized spheres until the spheres touch and bond permanently together into a well-defined cluster.<sup>5</sup> One could still define a center-of-mass for these PSCs, which would be equivalent to the center of mass of a core particle; thus the positions of core particles can describe the overall crystal structure of the system whether or not the core particles are actually present within the PSCs.

In this study we investigate purely repulsive Platonic PSCs, as shown in Fig. 1, and report the first finding of crystal structures self-assembled from them. We find remarkable complexity in the structures that assemble, with some PSCs demonstrating more than one phase depending upon the system volume fraction. We impose purely repulsive interactions between constituent PSC spheres, and thus produce results that are independent of absolute particle size, provided the diameter ratio of “halo” to “core” spheres remains fixed and the PSCs are Brownian. Our assemblies instead emerge primarily entropically from excluded volume effects of rigid colloidal building blocks, in the absence of any attractive forces. In the following sections, we describe and summarize our computational study.

## 2 Model

We utilize a minimal coarse-grained model used in previous works to study the assembly behavior of rigid colloidal particles.<sup>39,48–53</sup> The colloidal clusters are modeled as rigid bodies<sup>52</sup> composed of beads situated at the vertices of the Platonic polyhedra (the halo particles); an additional core particle, whose diameter is chosen to just touch the surrounding particles, is present at the center of each cluster. As mentioned earlier, the core particle has no influence on phase behavior since interactions are purely repulsive and the core particle is buried within the cluster so that it cannot interact repulsively with core or halo particles of any other cluster. For the icosahedral cluster, we choose the core and halo spheres to be all the same size, to match with a known experimentally achievable cluster geometry.<sup>30,45</sup> Due to the geometry of the icosahedron, this necessitates that the halo spheres do not actually lie completely tangent to each other. Rather, the edge length in this case is  $\frac{2\sigma}{\sqrt{\Phi}5^{1/4}} \sim 1.05\sigma$ , rather than  $\sigma$ , where  $\Phi$  is the golden ratio. For this reason, our icosahedral cluster does not quite meet the formal definition of a Platonic PSC, although we will continue to refer to it as one. All five PSCs – tetrahedron, cube, octahedron, icosahedron, and dodecahedron – are shown in Fig. 1; insets show the connectivity of the “halo” particles and the polyhedral cage.

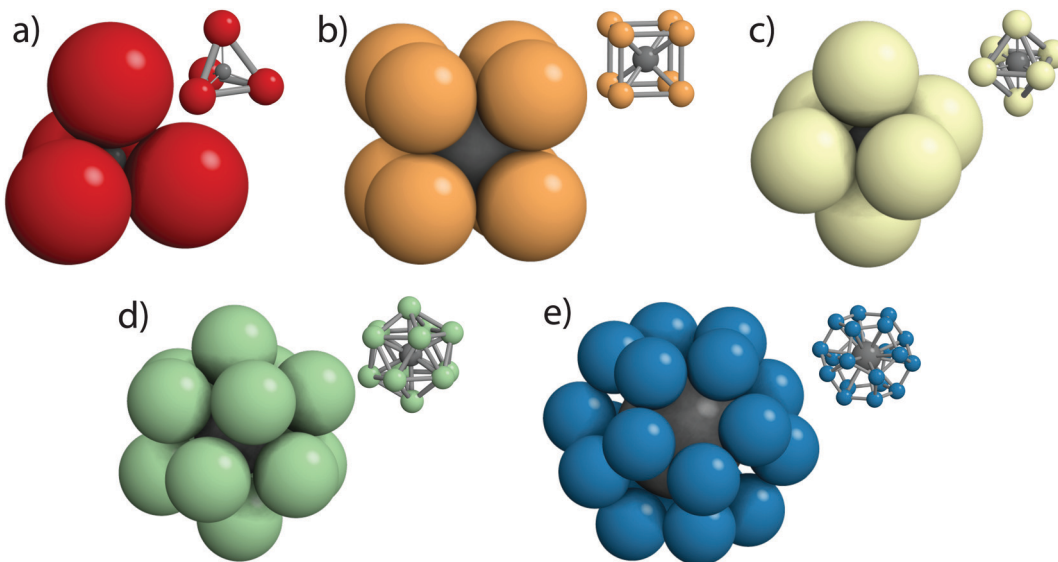


**Fig. 1** The polyhedral sphere cluster (PSC) geometries used in this study. All Platonic solids were simulated, and are depicted in order of increasing number of facets – (a) tetrahedron, (b) cube, (c) octahedron, (d) icosahedron, (e) dodecahedron. The polyhedral structure of each particle is inset in each panel; distances between spheres within each rigid body are fixed over the course of the simulation.

We use a Weeks–Chandler–Anderson (WCA) potential<sup>54</sup> to model repulsive interactions between constituent spheres on different PSCs. This potential is defined in the usual way by shifting the standard Lennard-Jones (LJ) potential upward in energy and truncating at its minimum so that it goes smoothly to zero at its cut-off. This shift results in an effective hard-sphere interaction, with little to no penetration of spheres in neighboring clusters except at extremely high densities beyond those studied here. The PSCs only interact *via* the individual repulsive potentials calculated pairwise between spheres on different PSCs. The self-assembled phases we report arise from these purely repulsive interactions, rather than *via* any sophistication in the design of the potential between PSCs. As a result, all self-assembly is driven essentially solely by entropy. Further detail on the WCA potential, including a plot of its functional form, is provided in the ESI.<sup>†</sup>

The PSCs are simulated in an implicit solvent within the *NVT* ensemble using Brownian dynamics (BD),<sup>55</sup> which avoids the need for modeling an explicit solvent and thus reduces the computational workload. Particle trajectories are governed by the Langevin equation,  $m\ddot{\mathbf{r}}_i(t) = \mathbf{F}_i^C(\mathbf{r}_i(t)) + \mathbf{F}_i^R(t) - \gamma\mathbf{v}_i(t)$ , where  $m$  is the particle's mass,  $\mathbf{r}_i$  is its position,  $\mathbf{F}_i^C$  is the conservative force on the particle,  $\mathbf{F}_i^R$  is a random force,  $\mathbf{v}_i$  is the particle velocity, and  $\gamma$  is the particle's friction coefficient. The friction coefficient is  $\gamma = 6\pi\eta\sigma$ , where  $\eta$  is the solvent viscosity.  $\mathbf{F}_i^C$  is the conservative force established by the WCA potential. The random force,  $\mathbf{F}_i^R$ , satisfies the fluctuation–dissipation theorem. The combined effect of the friction coefficient,  $\gamma$ , and the random force,  $\mathbf{F}_i^R$ , is to couple particles to a non-momentum-conserving heat bath. The dimensionless time is  $t = \sqrt{m\sigma^2/\epsilon}$ , where  $\epsilon$  sets the energy scale of the potential and other parameters are as previously defined. The system temperature is given by  $T^* = k_B T / \epsilon$ . The volume fraction,  $\phi$ , of the system is

determined by dividing the total excluded volume of all particles by the total volume of the box.

Simulations are initialized with  $N = 4096$  PSCs (aside from the dodecahedra, which are run with  $N = 1512$  and  $3600$ ) randomly placed in a cubic box with periodic boundary conditions; specific numbers of PSCs are listed in the results section. The system is randomized by thermalizing it at  $T^* = 1.0$ , for 1 million time steps. All simulations begin dilute, and are compressed to the desired volume fraction over  $10^6$  time steps by isotropically shrinking the box dimensions. Finally, the system is equilibrated at the final volume fraction by running for a number of time steps between  $\sim 1.9 \times 10^8$  and  $\sim 1 \times 10^9$ . All simulations use a time step  $\Delta t = 0.005\sqrt{m\sigma^2/\epsilon}$ . Every system is simulated over a range of volume fractions between  $\phi = 25\%$  and  $60\%$ ; specific information on each PSC is given in the “Results” section. Simulations are performed using the Highly Optimized Object-oriented Molecular Dynamics (HOOMD-blue software package,<sup>56</sup> a GPU-based Molecular Dynamics (MD) code. All clusters are treated as rigid bodies,<sup>52</sup> and thus the bonds within a cluster remain fixed over time.

The system pressure,  $P^*$ , is calculated *via* the virial stress tensor.<sup>57</sup> To determine equations of state, pressure data were taken from the final 10% of the run in all cases. We obtained statistically independent measurements by calculating the pressure autocorrelation function for each trajectory,  $r_p(\tau) = \frac{\langle (p(t) - \langle p \rangle)(p(t + \tau) - \langle p \rangle) \rangle}{\langle (p(t) - \langle p \rangle)^2 \rangle}$ .

The pressure autocorrelation is a function of the lag time  $\tau$  between pressure measurements, and is unity if pressures at any time  $t$  are perfectly correlated with those at  $t + \tau$ ,  $-1$  if they are perfectly anticorrelated, and  $0$  if they are uncorrelated. Brackets indicate averages taken over a dynamic trajectory, at every value of  $t$  for which system pressure was measured. We visually inspected  $r_p(\tau)$  for the final tenth of each trajectory, and chose a corresponding

conservative lag time  $\tau$ , specific to each trajectory, beyond which we determined by eye that  $r_p(\tau)$  had become distributed randomly about 0. We then used only pressure measurements spaced by these values of  $\tau$  in our calculations of average pressure for each state point and used the number of data points, taken as independent measures, to assess the mean pressure and its standard error.

All phases are identified through a combination of visual inspection of the structure as well as its calculated diffraction pattern, radial distribution function (RDF), and bond-orientational order diagram (BOD).<sup>58,59</sup> Structures are denoted by their Pearson symbols, consisting of a lower-case letter indicating the crystal system (*e.g.*, *c* for “cubic” in *cF4*), an upper case letter indicating the lattice centering (*e.g.*, *F* for “face-centered”), and a number indicating the number of particles per unit cell (*e.g.*, 4). In its long form it is combined with a prototype compound that adopts this structure (*e.g.*, Cu in *cF4-Cu*).

### 3 Results

Four of the five Platonic PSCs produced thermodynamically stable, or at least metastable, crystalline phases. Here we

describe the phases found in our simulations and the thermodynamic parameters at which they are found. We did not observe a tetrahedral PSC phase accessible *via* self-assembly, but we did observe that a constructed ordered crystal of tetrahedra remains stable under thermalization, and that a crystallographically related ordered crystal grows from a seed crystal; these points will be elaborated on in the “Discussion” section. All other Platonic PSCs (cube, octahedron, icosahedron, and dodecahedron) demonstrate one or more crystalline phases that are accessible *via* self-assembly following compression from the initial low-density, disordered state. Each of these systems is fluid at low  $\phi$ , crystallizes into one or more ordered phases at higher  $\phi$ , and in most cases remains disordered when compressed to the highest  $\phi$  investigated, failing to crystallize on the time scales of our simulations. Fig. 2 shows a variety of the self-assembled crystal structures obtained *via* simulation at intermediate  $\phi$  between these limits. Fig. 3 shows approximate equations of state, with all fluid and crystalline phases included, but excluding state points at high  $\phi$  for which the system failed to assemble into a crystalline structure on simulation timescales; in the equation of state, each data point is a

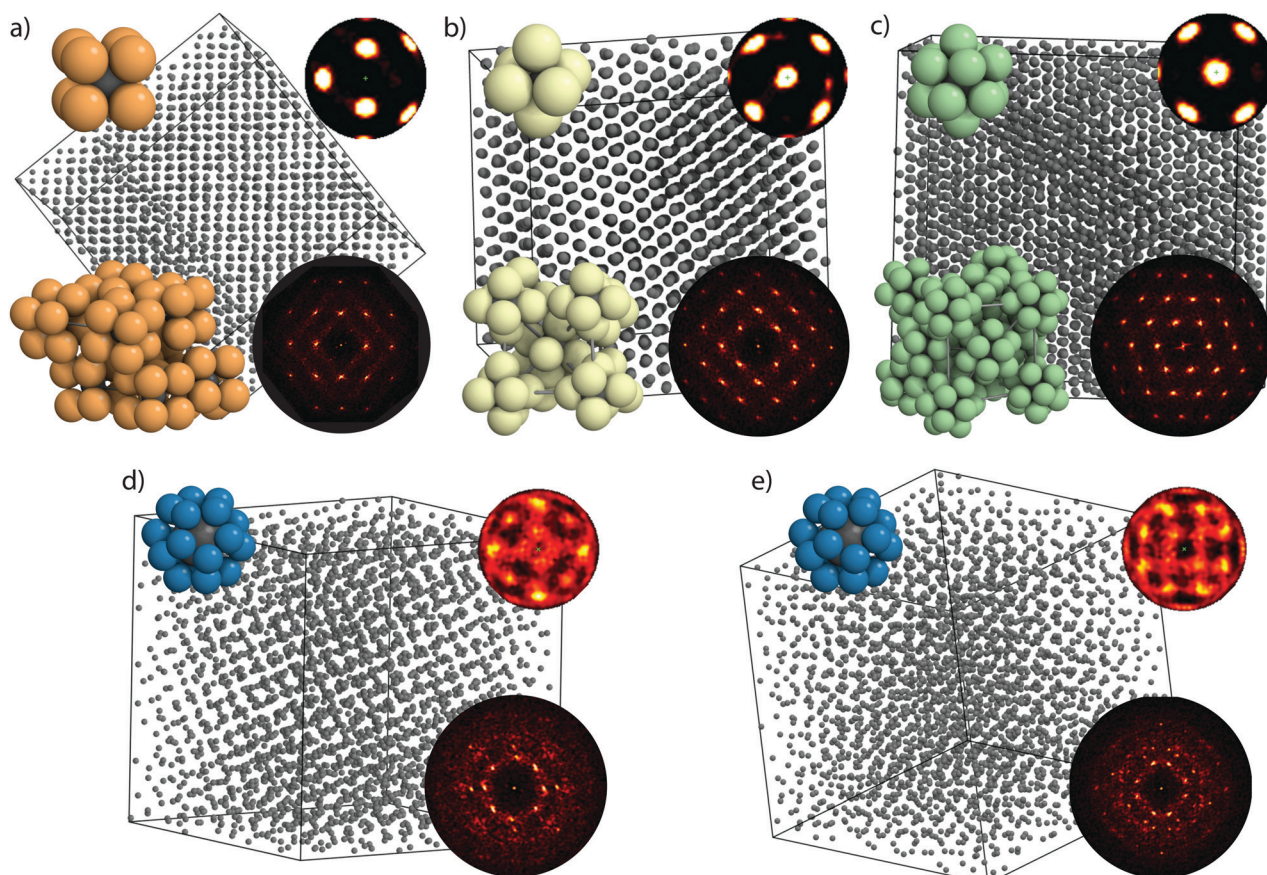


**Fig. 2** Results of various assemblies. In all assembly images only the core (center) spheres are shown, in gray, for clarity. Bond-orientational order diagrams (BODs) calculated for core spheres for each phase are located in the upper right corner of each panel, the Platonic PSC is shown in the upper left corner, and associated core sphere diffraction patterns are shown in the lower right corner. To demonstrate the packing of the full PSC, including halo spheres, panels (a–c) additionally show the full PSC unit cell in the lower left corner; in panels (d and e) the unit cells are omitted for clarity, due to their higher complexity. (a) *hR3* phase formed by cubes; (b) body-centered cubic (BCC; *cI2*) phase formed by octahedra; (c) face-centered cubic (FCC; *cF4*) phase formed by icosahedra; (d) *hP7* and (e) *cP20* phases formed by dodecahedra.

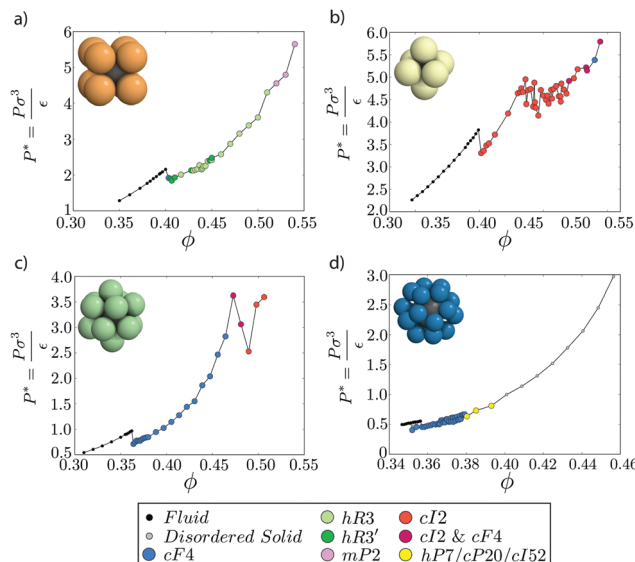


**Fig. 3** Equations of state for the four PSCs that readily self-assemble crystalline structures: (a) cube, (b) octahedron, (c) icosahedron, and (d) dodecahedron. Each state point corresponds to a separate simulation, and the system pressure,  $P^*$ , is calculated via the virial stress tensor. All plots contain error bars (representing the standard error of the mean of the pressure, collected over the course of a given run), but error bars are all smaller than the size of the symbols. Noise in the curves is the result of some systems not being homogeneously crystalline, possessing regions of defects. Lines are drawn as a guide to the eye, and do not represent exact phase boundaries.

separate simulation. To construct the equation of state each volume fraction was obtained as the final density after a relatively rapid compression from a dilute fluid system, as described above, to the desired final volume fraction. After this volumetric “quench”, the system was equilibrated for a prolonged time, during which crystallization might occur. We did not attempt to observe a solid–solid transition by gradually compressing the volume, but instead obtained a new volume fraction by carrying out a new simulation starting from a dilute concentration and compressing relatively quickly to the new volume fraction. The crystal structures discussed initially in the following paragraphs are based on the positions of the core spheres for each PSC. Because the tetrahedron was the only PSC that did not directly self-assemble we list results for this PSC last, after first reporting those that readily self-assembled from the fluid phase. We conclude the section with a summary of observed PSC halo sphere crystal structures.

### 3.1 Cubic PSC

The cubic PSC was run at 40 final volume fractions between  $\phi = 35\text{--}54\%$ , with  $N = 4096$  spheres, for  $500 \times 10^6$  timesteps. At low final volume fractions, as with all PSCs, the system is not sufficiently dense to crystallize. However, as a volume fraction of  $\phi = 40\%$  is approached, a phase transition to a FCC-type structure ( $cF4$ -Cu, or, for short,  $cF4$ ) occurs, where here and elsewhere we are referring to the structure of the core spheres, unless stated otherwise. Between  $\phi = 40.5\text{--}51\%$  the system

forms two different phases that are related to the hexagonal  $hR3$ -Po-type. Although the unit cell of  $hR3$ -Po has  $c/a \approx 1$ , the two structures observed here exhibit  $c/a \approx 0.8$  and  $c/a \approx 1.9$ , respectively, the latter dominating the phase region, while appearances of the former are scattered throughout the entire range of packing fractions. The low- $c/a$  phase is similar to the eponymous  $hR3$ -Po phase; both have coordination polyhedra (CP) (*i.e.*, the local environments of the core spheres of each PSC) that correspond to distorted octahedra, with coordination numbers CN = 6, but with another set of six neighbors at a similar distance. The coordination of the high- $c/a$  phase however is clearly CN = 12 and corresponds to a distorted cuboctahedron; it is therefore closely related to the FCC-type structure that forms at low packing fractions. The cubic PSCs form a configuration in which “faces” of the cubes do not prefer to align; instead, the system adopts a 3D interdigitated phase that best accommodates the packing of the halo spheres. Such interdigitation of cubes modeled by spheres has been previously observed in simulations.<sup>60</sup> At high values of  $\phi = 52\text{--}54\%$ , the cubic PSCs form a monoclinic phase ( $mP2$ ). The highest density phase observed for the cubic PSC is shown in Fig. 2a, and its equation of state is shown in Fig. 3a.

### 3.2 Octahedral PSC

The octahedral PSC was run at 60 volume fractions between  $\phi = 39\text{--}56\%$ , with  $N = 4096$  spheres, for  $500 \times 10^6$  time steps. Up to  $\phi = 45\%$ , no crystallization occurs and the system remains in the fluid state. Above this volume fraction, but below  $\phi = 51\%$ , the system forms a BCC structure ( $cI2$ -W), which is shown in Fig. 2b. The CP for the  $cI2$ -phase is a rhombic dodecahedron (or a combined cube and octahedron). At the higher values of  $\phi = 51\text{--}55\%$ , the system forms either a  $cI2$ , a  $cF4$  phase, or both phases ( $cI2$  and  $cF4$ ) coexist simultaneously within a single simulation box; thus both phases are at least metastable at these volume fractions. The equation of state for the octahedral PSC is shown in Fig. 3b.

### 3.3 Icosahedral PSC

The icosahedral PSC was run at 40 volume fractions between  $\phi = 35\text{--}54\%$ , with  $N = 4096$  spheres, for  $500 \times 10^6$  time steps. At volume fractions of  $\phi = 36\%$  and below, the system is a fluid. At volume fractions between  $\phi = 36.4\text{--}47.3\%$  the system forms the FCC structure ( $cF4$ ); this phase is shown in Fig. 2c. The CP for the  $cF4$  phase is a cuboctahedron. At volume fractions of  $\phi = 48.1\text{--}50.6\%$  the system forms  $cI2$ . Between  $\phi = 47.3\text{--}48.1\%$  a mixture of  $cI2$  and  $cF4$  occurs. The equation of state for the icosahedral PSC is shown in Fig. 3c.

### 3.4 Dodecahedral PSC

The dodecahedral PSC was run at 72 volume fractions between  $\phi = 34\text{--}52\%$ , with  $N = 1512$  spheres, for  $1000 \times 10^6$  timesteps; an additional set of runs was performed at 10 volume fractions in the range  $\phi = 30\text{--}43\%$  with  $N = 3600$  for  $500 \times 10^6$  timesteps. As with all clusters, at low volume fractions ( $\phi < 35.7\%$ ) the system is a fluid. Between volume fractions of  $\phi = 35.7\text{--}36.6\%$

the core spheres adopt a FCC configuration (*i.e.*, *cF4*). While FCC still dominates at higher concentrations, multiple competing phases for the cores are observed in the range  $\phi = 36.7\text{--}39.3\%$ : the so-called  $\gamma$ -brass phase, *cI52*-Cu<sub>5</sub>Zn<sub>8</sub>, the  $\beta$ -manganese structure, *cP20*-Mn, and the topologically close-packed Frank-Kasper phase *hP7*-Zr<sub>3</sub>Al<sub>4</sub>. The CPs of all these structures have 12 to 15 vertices and are reminiscent of icosahedra or other Frank-Kasper polyhedra typically found in intermetallic compounds. The *hP7* and *cP20* structures are shown in Fig. 2d and e respectively; images displayed are from the  $N = 3600$  PSC runs. The equation of state for the dodecahedral PSC is shown in

Fig. 3d, with all data points taken from the  $N = 1512$  PSC runs. Additionally, as shown in the lower left portion of Fig. 3d, at two volume fractions FCC crystals were found within what was otherwise a region of fluid. To investigate, we performed a series of 10 independent melting simulations in which we isotropically expanded all box edges ( $L = 1.0\text{--}1.125x$ ) from the structure obtained *via* self-assembly at  $\phi = 35.2\%$ . The FCC structure was stable down to a volume fraction of  $\phi = 30.51\%$ , melting for lower values of  $\phi$ ; this indicates that the structure is at least thermodynamically metastable, but difficult to access at low  $\phi$ .

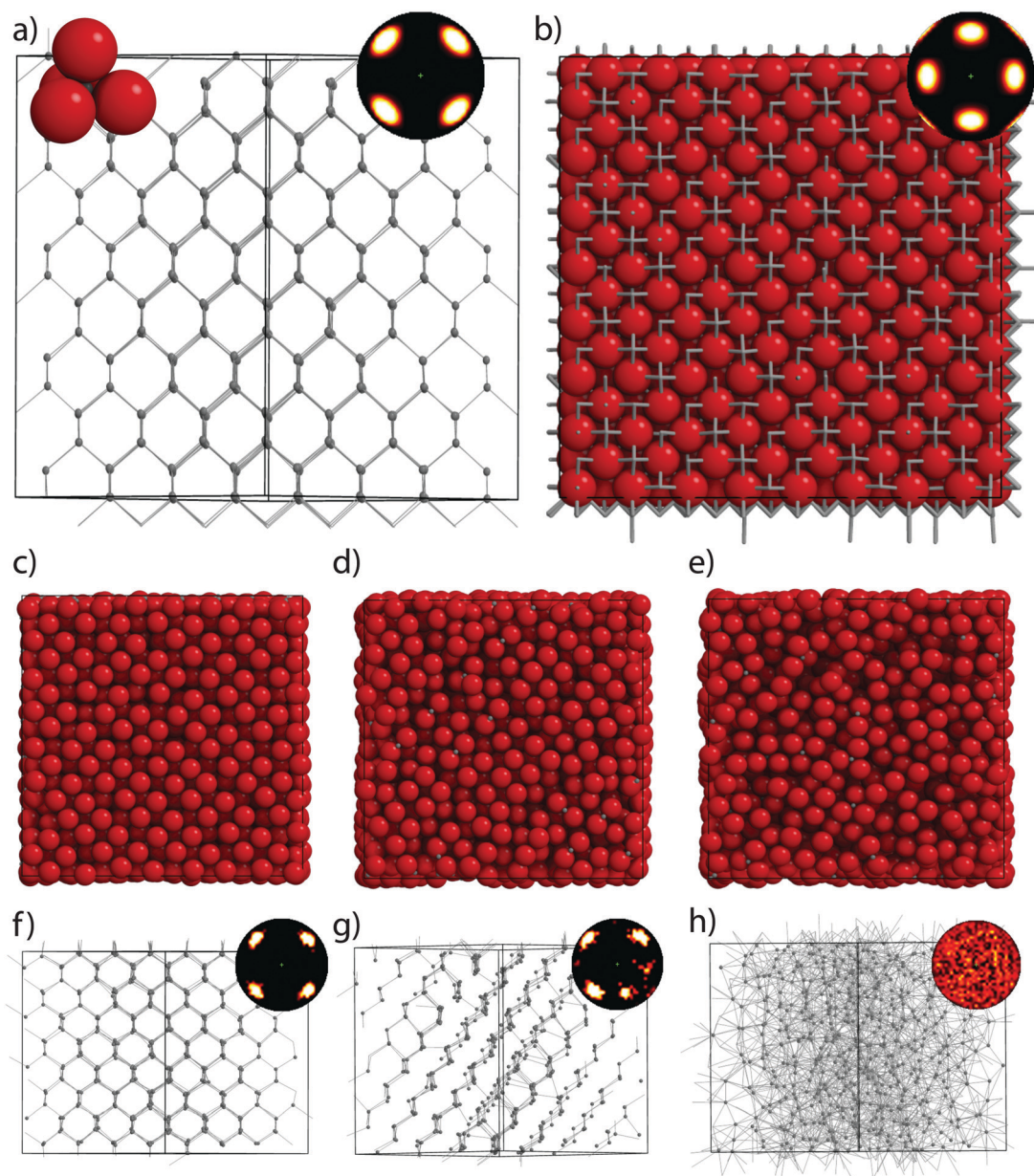


**Fig. 4** Diamond crystal melting runs from a perfect crystal. The top row shows the constructed diamond crystal cores, (a), and halo spheres, (b). The middle row shows a series of volume fractions run from, (c and f), the perfect *cF8*-crystal to, (d and g), a partially melted transition structure (with Pearson symbol *hP2*, and space group *P3m1*) to finally, (e and h), a fully melted structure. The bottom row shows the corresponding core spheres, with bonds drawn out to the first peak of the radial distribution function (RDF). The BODs for the structures are shown in the top and bottom rows.

### 3.5 Tetrahedral PSC

For the tetrahedral PSCs, self-assembly studies produced no ordered crystalline phases over a range of volume fractions  $\phi = 35\text{--}60\%$ . This region was targeted specifically because it is known that there are feasible crystalline packings of tetramers in this range of volume fractions<sup>61</sup> where the halo spheres of the tetramer adopt a FCC packing, while the core spheres can adopt a different, but commensurate, diamond (*cF8*) packing. This construction is shown in Fig. 4a and b.

To test the stability of the pre-assembled tetrahedral PSC system, we constructed the diamond/FCC packing of PSCs by hand and performed melting studies. The system shown in Fig. 4a and b was created in such a way that halo spheres are

just touching, but do not overlap. Melting runs were performed by resizing the box isotropically in all directions to the chosen volume fraction over  $10^5$  time steps, and then equilibrating for  $100 \times 10^6$  time steps; 15 volume fractions were chosen linearly spaced between  $\phi = 44.07\text{--}74.26\%$ . The results show that the diamond/FCC structure remains stable at volume fractions in the range of  $\phi = 54.3\text{--}74.26\%$ , while completely melting for volume fractions below  $\phi = 48.82\%$ ; in between, a transition crystal related to the diamond structure *via* an elongation in the *z*-direction with Pearson symbol *hP2* appears. This structure appears despite the fact that the box resize was isotropic, so this elongation represents a symmetry breaking in the system. Three example phases are shown in Fig. 4c–h: the first is the

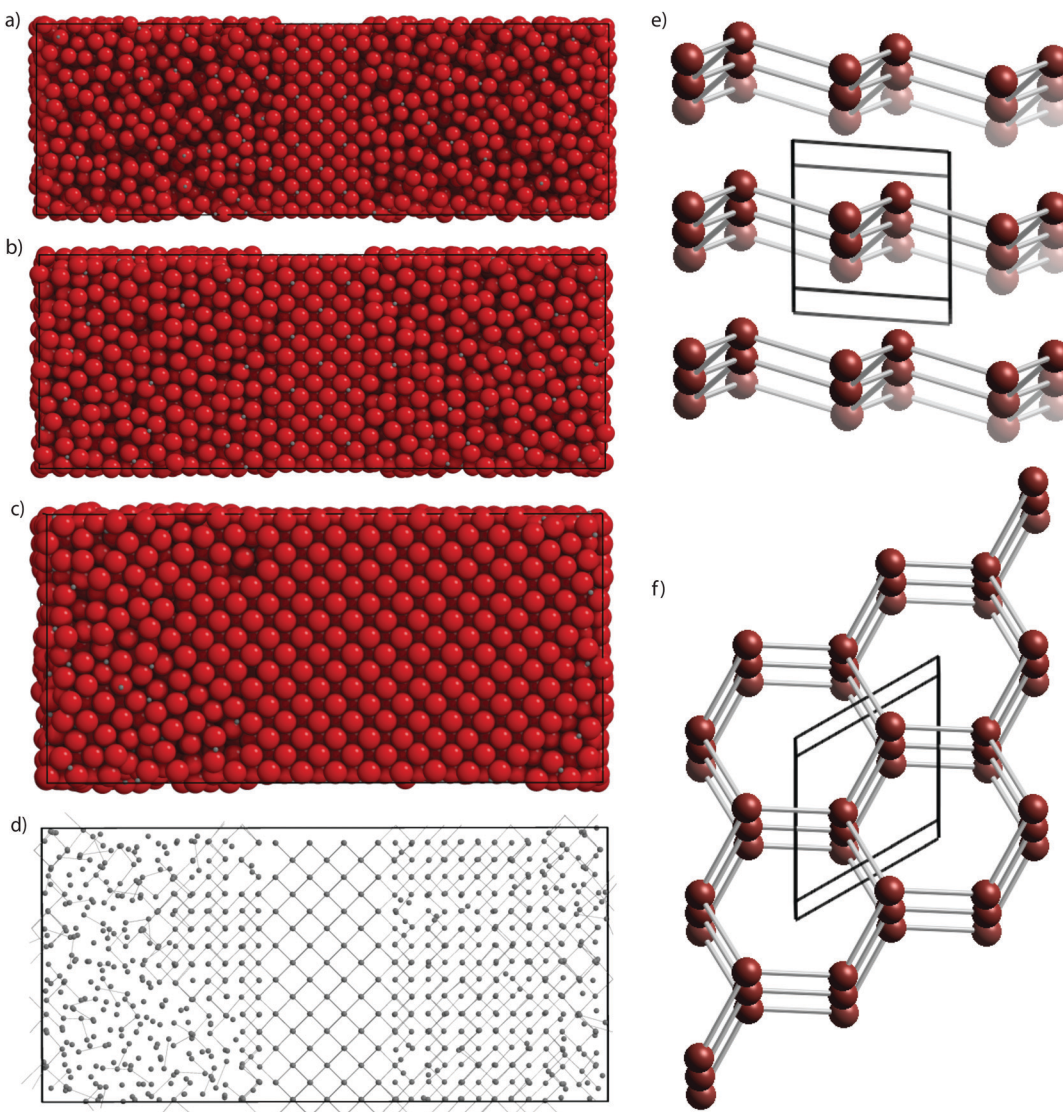


**Fig. 5** Example snapshots taken from seeded melting runs. A seed layer of  $\frac{2}{5}$  of the box was frozen, while the remaining PSCs were melted by increasing the *x*-axis, and equilibrating the non-frozen tetrahedral PSCs. The box was then resized over  $500 \times 10^6$  timesteps, and further equilibrated for  $500 \times 10^6$  timesteps. The subfigures show stages where, (a) the non-frozen beads have melted, (b) the structure has begun to re-crystallize, and (c) re-crystallization has progressed farther. In (d) just the cores from (c) are shown, with bonds drawn corresponding to the first peak of the RDF. The unit cell for the new structure is shown from two directions in the right column, panels (e) and (f): the *hP2*-structure is related to diamond, but with a slightly elongated *z*-axis that breaks connections between layers of the structure.

constructed crystal, the second is the transition *hP2* crystal, and the third is the fluid; also pictured are just the core spheres and bonds drawn out to the first peak of the radial distribution function (RDF).

We further investigated the robustness of the diamond crystal by performing seeded crystal runs. In these runs, a thin slab of the diamond/FCC crystal (3 to 4 tetrahedra thick) was left frozen at the center of the box. The non-frozen portion of the crystal was melted by extending the length of the box in the [100]-direction, and allowing the PSCs to equilibrate. The system was then re-compressed to between 1–1.125 $x$  of its original length along [100] over  $500 \times 10^6$  time steps, and then further equilibrated for an additional  $500 \times 10^6$  time steps. An example of this is shown in Fig. 5a–d. The structure is observed to recrystallize into the *hP2* phase. Fig. 5d shows the arrangement of the core spheres, and the unit cell of the new crystal is inset at the lower left. This *hP2* crystal has the same structure as that obtained by partially melting the perfect diamond crystal, shown in Fig. 4d, indicating that this phase is at least metastable over a finite range of volume fractions.

### 3.6 Halo sphere crystals

Finally, Fig. 6 summarizes the observed PSC halo sphere crystal structures, along with the corresponding crystal structures observed in the core spheres for all five Platonic PSCs. It is important to note that the halo spheres did not crystallize as readily as their cores – meaning that in some cases, while the core spheres formed an ordered structure, their halo spheres

did not. In all cases where both the core and halo spheres crystallized a given crystalline arrangement of the core spheres produced only one corresponding crystalline arrangement of halo spheres. For the tetrahedral PSCs, all reported phases contained halo spheres arranged on a FCC (*cF4*) lattice, while core spheres occupied either a *cF8* or an *hP2* structure. For the cubic PSCs, halo spheres were arranged on a *cP1* lattice when the core spheres occupied a FCC (*cF4*) lattice; additionally, halo spheres were found to correspond to a *tI8* structure when core spheres were positioned in an *hR3* structure. For the octahedral PSCs, halo spheres were arranged on a FCC (*cF4*) lattice when the core spheres occupied a BCC (*cI2*) lattice. For the icosahedral PSCs, halo spheres were arranged in a *cI24* structure when the core spheres occupied a BCC (*cI2*) lattice. For the dodecahedral PSCs, halo spheres were arranged on a BCC lattice (*cI2*) when the core spheres occupied a FCC (*cF4*) lattice; additionally, halo spheres were found to lie on a FCC (*cF4*) lattice when core spheres formed a *cI52* structure.

## 4 Discussion

Our simulations demonstrate that, aside from the tetrahedron, all purely repulsive Platonic polyhedral sphere clusters self-assemble into one or more ordered phase(s). Despite the simplicity and difference in geometry of the PSCs relative to their polyhedral counterparts, we report here that some of their assemblies are similar to those formed by faceted polyhedra.<sup>5,40,41,43,62,63</sup>

The following phases have been reported for hard Platonic polyhedra:<sup>41</sup> *cP1-Po* for cubes, *hR3-X* for octahedra, *cF4-Cu* for icosahedra, and *cP20-Mn* for dodecahedra. While the self-assembled structures observed in systems of faceted polyhedra also occur in the self-assembly simulations of PSCs for dodecahedra and icosahedra, the octahedral PSCs assemble a higher-symmetry version of the structure formed by their faceted counterparts (*cI2-W*), and the structures in the cubic system differ even more. Table 1 summarizes results for the self-assembly of hard Platonic polyhedra and the PSC polyhedra investigated in this paper.

This relationship between crystals formed by the PSCs and their purely polyhedral counterparts can be exploited by experimentalists for whom the construction of faceted particles is difficult or expensive, but the assembly of polyhedral clusters of spheres is easier. Furthermore, in any given assembled structure, the halo and core particles form distinct, albeit related, structures – a fact that can be exploited to design specific crystals such as the previously mentioned photonically relevant diamond structure. Such an approach is conceptually similar to the use of polyhedral DNA cages to assemble colloidal spheres in a diamond structure.

**Fig. 6** Table of BODs for assembled crystal structures of all five PSCs. For each PSC, the corresponding Pearson symbol, first for structures formed by the core spheres and last for structures formed by the halo spheres, is given. In between, the core–core, core–halo, and halo–halo BODs are given. For the Pearson symbol column, each symbol corresponds to the similarly positioned BODs in subsequent columns. (a) The seeded tetrahedral PSC structures, and structures self-assembled by the (b) cubic PSC, (c) octahedral PSC, (d) icosahedral PSC, and (e) dodecahedral PSC. In the case of the tetrahedral PSC (a), halo spheres are arranged on a FCC (*cF4*) lattice. For the icosahedral PSC (d), halo spheres are observed to crystallize readily.

**Table 1** Platonic polyhedra phases – faceted vs. PSC

Shape	Faceted polyhedron	PSC polyhedron
Cube	<i>cP1-Po</i>	<i>cF4-Cu hR3-Po</i>
Octahedron	<i>hR3-X</i>	<i>cI2-W cF4-Cu</i>
Icosahedron	<i>cF4-Cu</i>	<i>cF4-Cu cI2-W</i>
Dodecahedron	<i>cP20-Mn</i>	<i>cF4-Cu cP20-Mn cI52-Cu<sub>5</sub>Zn<sub>8</sub> hP7-Zr<sub>3</sub>Al<sub>4</sub></i>

Of the five Platonic PSCs, all except the cube and dodecahedron have been experimentally realized.<sup>30,45,64</sup> Thus, structures formed by sharp, faceted polyhedral particles can be made accessible to experimentalists for whom the construction of these particles is difficult or undesirable, since similar structures are also formed by assemblies of PSCs.

We have observed a wide diversity of ordered crystal structures formed as determined by the positions of the core particles in each PSC. Cubic, icosahedral, and dodecahedral PSCs all assemble into the sphere-packing *cF4* at low packing fractions, their behavior approaching that of spherical shapes in that regime. Dodecahedral PSCs form *cF4* at lower packing fractions and a series of other structure types typical of intermetallic compounds at higher packing fractions: gamma brass (*cI52*), beta manganese (*cP20*), as well as the Frank-Kasper phase *hP7*. All of these structure types have similar coordination numbers and while their local motifs are distinct and are all clearly observed, the formed global structures in these simulations are somewhat ambiguous. In most cases the halo spheres also arrange into a periodic structure. The halo spheres necessarily sit in locations that are complementary to the structure formed by the core particles, effectively in the interstices of the core–core crystal structure. Fig. 6 illustrates this for all five Platonic PSCs: core–halo BODs (formed by mapping the positions of the halo spheres with respect to their associated core particle onto the surface of a sphere) are essentially dual to core–core BODs (formed by mapping the positions of the core particles with respect to their nearest core–particle neighbors onto the surface of a sphere), signifying that halo spheres occupy positions that are interstitial in the core–core crystals.

As we reported in the “Results” section, we observed that the interstitial placement of the halo spheres with respect to the core–core crystal structure caused nested crystals to emerge, in which the core particle of the PSC arranges in one structure, while the halo spheres adopt a different one. Examples can be seen in Fig. 7 for the octahedra and icosahedra and in Fig. 4 for the tetrahedra. For the tetrahedral PSC, core particles form a diamond (*cF8*) structure while halo spheres form an FCC (*cF4*) structure, Fig. 4; for the octahedral PSC, core particles form a BCC-like (*cI2*) structure while halo spheres form an FCC-like (*cF4*) structure, Fig. 6c; and for the icosahedral PSC, core particles form a BCC (*cI2*) structure while the halo spheres decorate a complex structure where the PSCs stack in columns and spheres have a fixed twist with respect to the column axis, Fig. 6d.

We found the structural relationship between the halo particles and the core particles of the octahedral PSC to be of particular interest. We observed a shift in cluster orientations that took place concurrently with a phase transition from one solid core–core crystal structure to another; this process is depicted in detail in Fig. 8. To better understand this transition, we investigated relative cluster orientation *via* computing the set of minimal angles through which each cluster must be rotated such that it is oriented in the same direction as each of its  $N$  nearest neighbors. We averaged this set of minimal angles for  $N = 14$ , producing an average minimal angle per cluster.

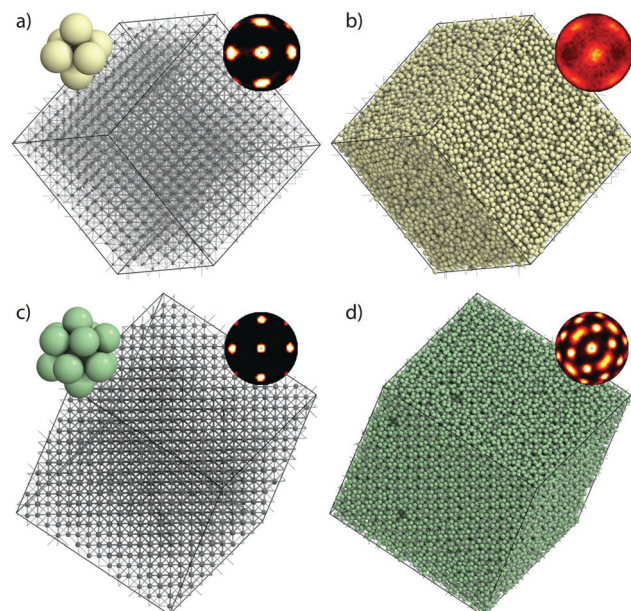
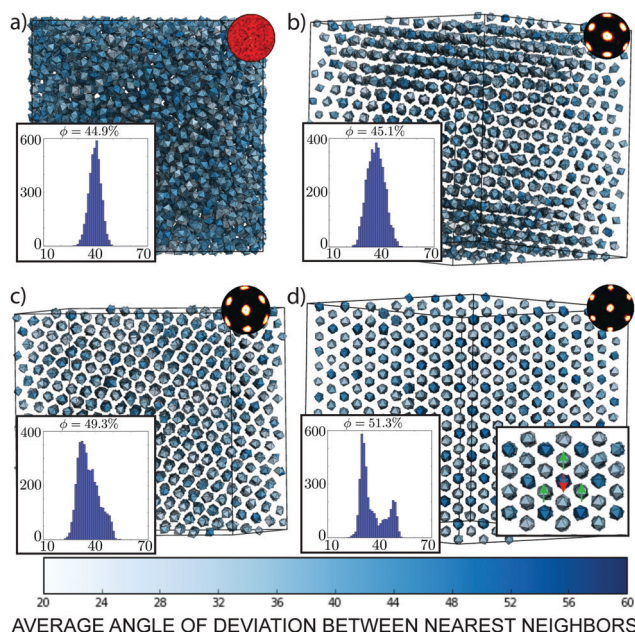


Fig. 7 Nested crystal assemblies. The top row shows the octahedral PSC: (a) “cores” adopt a *cI2* configuration, while (b) “halos” adopt a BCC-like configuration. The bottom row shows the icosahedral PSC: (c) “cores” also adopt a *cI2* configuration, while (d) “halo” spheres additionally order, all adopting the same orientation in the *cI2* lattice. BODs are shown in the upper right corner of all subfigures, while the PSCs are depicted for each shape in subfigures (a) and (c).

Cluster symmetry was taken into account: we regarded all halo spheres as indistinguishable, and thus the octahedral PSC had a set of “equivalent orientations,” or rotations that resulted in clusters that were identical for the purposes of this study. The minimal angle calculated for each cluster pair is the smallest angle of rotation among all equivalent orientations of both clusters. Note that the nature of the angular distribution of randomly sampled rotations, in addition to the underlying cluster symmetry, means that the distribution of the average minimal rotation angle between an orientation chosen randomly and a set of 14 orientations also chosen randomly is not flat. Rather, it is peaked around  $\theta \sim 41^\circ$  and has the shape displayed in ESI† Fig. S2.

Distributions of per-cluster average minimal angles to neighboring clusters for various system densities are shown in Fig. 8, along with accompanying simulation snapshots (with particles rendered as perfect polyhedra and colored by average minimal angle to  $N = 14$  nearest neighbors for convenience and clarity) and corresponding BODs. As would be expected, at low densities the system is disordered, as evidenced by both the coloration of the particles and the uniformity of the BOD (see Fig. 8a). The distribution of average minimal angles is peaked at around  $40^\circ$ , which is close to the peak of the random distribution described in the previous paragraph and shown in ESI† Fig. S2. At intermediate values of  $\phi$ , the system begins to crystallize, as seen in Fig. 8b. Several indicators mark this transition: first, the BOD now has regular peaks (indicative of a BCC structure), rather than a uniform pattern. Second, the peak of the average minimal angle distribution shifts below  $40^\circ$ ,



**Fig. 8** Phases of octahedral PSCs, demonstrating the orientational correlation between PSCs that arises as the system's final volume fraction is increased; each panel is a separate simulation performed at the volume fraction indicated in the insets. (a) Low volume fraction that does not crystallize ( $\phi = 44.9\%$ ). (b) Intermediate volume fraction chosen just within the crystalline region  $c/2$  ( $\phi = 45.1\%$ ). (c) High volume fraction chosen just prior to the order–order transition ( $\phi = 49.2\%$ ). (d) High volume fraction after transition into a second solid phase,  $cF4$  ( $\phi = 51.3\%$ ). Clusters are colored according to the ‘average angle of deviation between nearest neighbors’, or minimal angle through which they must be rotated to match the orientations of their nearest neighbors, averaged over 14 nearest neighbors for each cluster. Additionally, clusters are rendered as perfect polyhedra, where the vertices of each polyhedron are placed at the centers of the halo spheres of the PSC, and the center of each polyhedron is placed at the center of the core sphere of the PSC. The BOD along the  $\bar{3}$ -axis of the crystal is also shown for each system, along with a histogram of the average angle of deviation between nearest neighbors for every particle in the system snapshot.

indicating a deviation from random orientational correlation between clusters and their nearest neighbors.

As  $\phi$  increases, the orientational correlation between the clusters increases, as seen both in the coloration of the particles in Fig. 8c and the shift of the peak of average minimal angle to lower and lower values. Additionally, a second peak at higher values begins to emerge in the distribution of average minimal angles. Finally, at the highest values of  $\phi$  in our study, a bimodal distribution of particle orientations is readily apparent, reflected in both the distribution of average minimal angle and the crystal structure displayed in Fig. 8d. In this structure, all particles in a column along the  $\bar{3}$ -axis prefer to align. Furthermore, there are two ‘types’ of orientations that can readily be seen in the triangular faces of the octahedra. The faces point either up or down in the plane perpendicular to the  $\bar{3}$ -axis; ‘down’ orientations are always surrounded by 6 ‘up’ orientations, while ‘up’ orientations are always surrounded by 3 ‘down’ and 3 ‘up’ orientations. The inset of Fig. 8d is marked with ‘up’ (green) and ‘down’ (red) arrows to further illustrate this behavior.

The observed stability of the diamond/FCC structure is of significant technological importance, as an open diamond structure is known to possess a meaningful photonic band gap, a feature that is crucial for photonic devices.<sup>11,12</sup> Because of the core/halo arrangement of the PSCs, this allows for two types of spheres that can be chemically distinct. Such an arrangement has been pursued for over a decade, and has only recently been demonstrated in two separate realizations of DNA-bonded sphere clusters.<sup>17,29</sup> In the first case, a binary system of tetramers and spheres are used;<sup>29</sup> in the second case, a binary system of spheres using grafted single-stranded DNA is used.<sup>17</sup> The first experimental system maps directly to our tetrahedral PSC,<sup>30,45,64</sup> but with an additional sphere to create a binary superlattice corresponding to crystal structure  $cF24\text{-MgCu}_2$ ; taken separately, the tetramers were observed to form a pyrochlore structure, while the spheres form a diamond structure.<sup>17</sup> Thus, these structures are immediately realizable in the lab, and are ready to be tested for application and potential future integration into devices.

## 5 Conclusion

We simulated the self-assembly and crystallization behavior of all five Platonic sphere clusters. These PSCs possess no interaction aside from short-range repulsion, and show a diverse entropy-driven assembly behavior that emerges from the shapes of the various clusters. The types of crystal structures that form range from simple phases like FCC to complex ones such as the  $\beta\text{-Mn}$  structure. In general, our work shows a wealth of phases that can be obtained from simple sphere clusters made from particles with repulsive interactions alone. Since multiple methods are now available for making such clusters, their self-assembly without the aid of DNA bridging or other directional or attractive forces suggests a convenient way of realizing numerous complex solid phases using relatively simple physical chemistry.

We also investigated the relationship between the core–core assembled crystal structures and the location of the halo spheres in all assemblies. We find that the halo spheres occupy interstitial locations in the core–core assembled structures, demonstrated by the duality between the core–halo bond-order diagrams and the core–core bond-order diagrams of our simulations. The positions of the halo spheres can sometimes be extremely well-ordered and easy-to-access, as in the case of the icosahedra, but are frequently frustrated resulting in structures that contain defects or are less-ordered in general (as demonstrated by the halo–core and halo–halo bond-order diagrams in Fig. 6). Why some of these clusters so readily crystallize both halo and core spheres is not addressed in this work, and is an open area for further studies.

Finally, we described the thermodynamic stability of a diamond (core)/FCC (halo) structure made from tetrahedral PSCs. While the nested diamond/FCC phase was not directly accessible from the fluid phase *via* our purely repulsive model, it was stable when constructed. Furthermore, seeded crystal simulations grew a stable  $hP2$  phase that is a lower-symmetry

version of the diamond structure. Why the pre-constructed crystal is stable, but yet neither accessible *via* self-assembly from the fluid nor able to be grown by seeding the fluid is a compelling research question for future studies. Nonetheless, our findings are encouraging in that they suggest that further modifications to the interactions or the arrangements of the particles in the PSC may be able to fully stabilize the diamond/FCC arrangement. More generally, the large number of crystal structures accessible with just a small sampling of polyhedral sphere clusters (the Platonic PSCs) indicates the enormous range of structures likely available when other PSCs, such as those based on Archimedean, Johnson, or other polyhedra, are considered. In addition, our work indicates the intriguing possibility of creating nested crystals of halo spheres within crystals of core spheres, opening up a rich direction for colloidal self-assembly. All of this is possible using the simplest building blocks, *i.e.*, spheres, and purely repulsive interactions.

## Conflicts of interest

There are no conflicts to declare.

## Acknowledgements

RGL and RLM acknowledge support from the National Science Foundation under the grant CDS&E – 1602183. EGT acknowledges support through the National Science Foundation Graduate Research Fellowship Grant DGE 1256260 and a Blue Waters Graduate Fellowship. JD acknowledges support through the Early Postdoc.Mobility Fellowship from the Swiss National Science Foundation, grant number P2EZP2\_152128. This work was partially supported by a Simons Investigator award from the Simons Foundation to Sharon Glotzer (256297, SCG, JD, EGT). Computational resources and services were supported by Advanced Research Computing at the University of Michigan, Ann Arbor. The authors are grateful to Prof. Michael Engel for the use of inJaVis, the visualization tool used to produce images of the PSCs and their respective BODs.

## Notes and references

- S. C. Glotzer and M. J. Solomon, *Nat. Mater.*, 2007, **6**, 557–562.
- F. Li, D. P. Josephson and A. Stein, *Angew. Chem., Int. Ed.*, 2011, **50**, 360–388.
- O. Kruglova, P.-J. Demeyer, K. Zhong, Y. Zhou and K. Clays, *Soft Matter*, 2013, **9**, 9072–9087.
- N. Vogel, M. Retsch, C.-A. Fustin, A. del Campo and U. Jonas, *Chem. Rev.*, 2015, **115**, 6265–6311.
- V. N. Manoharan, *Science*, 2015, **349**, 1253751.
- M. A. Boles, M. Engel and D. V. Talapin, *Chem. Rev.*, 2016, **116**, 11220–11289.
- A. A. Shah, M. Ganesan, J. Jocz and M. J. Solomon, *ACS Nano*, 2014, **8**, 8095–8103.
- V. Saranathan, C. O. Osuji, S. G. J. Mochrie, H. Noh, S. Narayanan, A. Sandy, E. R. Dufresne and R. O. Prum, *Proc. Natl. Acad. Sci. U. S. A.*, 2010, **107**, 11676–11681.
- M. Kolle, P. M. Salgad-Cunha, M. R. J. Scherer, F. Huang, P. Vukusic, S. Mahajan, J. J. Baumberg and U. Steiner, *Nat. Nanotechnol.*, 2010, **5**, 511–515.
- G. E. Schröder-Turk, S. Wickham, H. Averdunk, F. Brink, J. D. Fitz Gerald, L. Poladian, M. C. J. Large and S. T. Hyde, *J. Struct. Biol.*, 2011, **174**, 290–295.
- M. Maldovan, C. K. Ullal, W. C. Carter and E. L. Thomas, *Nat. Mater.*, 2003, **2**, 664–667.
- M. Maldovan and E. L. Thomas, *Nat. Mater.*, 2004, **3**, 593–600.
- T. T. Ngo, C. M. Liddell, M. Ghebrebrhan and J. D. Joannopoulos, *Appl. Phys. Lett.*, 2006, **88**, 241920.
- A.-P. Hynninen, J. H. J. Thijssen, E. C. M. Vermolen, M. Dijkstra and A. van Blaaderen, *Nat. Mater.*, 2007, **6**, 202–205.
- W. Liu, M. Tagawa, H. L. Xin, T. Wang, H. Emamy, H. Li, K. G. Yager, F. W. Starr, A. V. Tkachenko and O. Gang, *Science*, 2015, **351**, 582–586.
- G. Avvisati, T. Dasgupta and M. Dijkstra, *ACS Nano*, 2017, **11**, 7702–7709.
- É. Ducrot, M. He, G.-R. Yi and D. J. Pine, *Nat. Mater.*, 2017, **16**, 652–657.
- R. K. Cersonsky, J. Dshemuchadse, J. Antonaglia, G. van Anders and S. C. Glotzer, *Phys. Rev. Mater.*, 2018, **2**, 125201.
- A. Klinkova, R. M. Choueiri and E. Kumacheva, *Chem. Soc. Rev.*, 2014, **43**, 3976–3991.
- Y. Wang, Y. Wang, D. R. Breed, V. N. Manoharan, L. Feng, A. D. Hollingsworth, M. Weck and D. J. Pine, *Nature*, 2012, **491**, 51–55.
- H. C. Shum, A. R. Abate, D. Lee, A. R. Studart, B. Wang, C. H. Chen, J. Thiele, R. K. Shah, A. Krummel and D. A. Weitz, *Macromol. Rapid Commun.*, 2010, **31**, 108–118.
- S. Sacanna, D. J. Pine and G.-R. Yi, *Soft Matter*, 2013, **9**, 8096–8106.
- T. C. Hales, S. P. Ferguson and J. C. Lagarias, *The Kepler Conjecture*, Springer, 2011, p. 456.
- N. Arkus, V. N. Manoharan and M. P. Brenner, *Phys. Rev. Lett.*, 2009, **103**, 118303.
- G. Meng, N. Arkus, M. P. Brenner and V. N. Manoharan, *Science*, 2010, **327**, 560–563.
- M. N. O'Brien, H.-X. Lin, M. Girard, M. Olvera de la Cruz and C. A. Mirkin, *J. Am. Chem. Soc.*, 2016, **138**, 14562–14565.
- M. T. Casey, R. T. Scarlett, W. B. Rogers, I. Jenkins, T. Sinno and J. C. Crocker, *Nat. Commun.*, 2012, **3**, 1209.
- Y. Wang, Y. Wang, X. Zheng, É. Ducrot, J. S. Yodh, M. Weck and D. J. Pine, *Nat. Commun.*, 2015, **6**, 7253.
- Y. Wang, I. C. Jenkins, J. T. McGinley, T. Sinno and J. C. Crocker, *Nat. Commun.*, 2017, **8**, 14173.
- J. T. McGinley, Y. Wang, I. C. Jenkins, T. Sinno and J. C. Crocker, *ACS Nano*, 2015, **9**, 10817–10825.
- M. B. Zanjani, I. C. Jenkins, J. C. Crocker and T. Sinno, *ACS Nano*, 2016, **10**, 11280–11289.
- S. Sacanna and D. J. Pine, *Curr. Opin. Colloid Interface Sci.*, 2011, **16**, 96–105.
- D. Nykypanchuk, M. M. Maye, D. van der Lelie and O. Gang, *Nature*, 2008, **451**, 549–552.

- 34 J. D. Halverson and A. V. Tkachenko, *Phys. Rev. E: Stat., Nonlinear, Soft Matter Phys.*, 2013, **87**, 062310.
- 35 Y. Zhang, F. Lu, K. G. Yager, D. van der Lelie and O. Gang, *Nat. Nanotechnol.*, 2013, **8**, 865–872.
- 36 Y. Tian, Y. Zhang, T. Wang, H. L. Xin, H. Li and O. Gang, *Nat. Mater.*, 2016, **15**, 654–661.
- 37 O. Gang and A. V. Tkachenko, *MRS Bull.*, 2016, **41**, 381–387.
- 38 M. N. O'brien, M. Girard, H.-X. Lin, J. A. Millan, M. Olvera De La Cruz, B. Lee and C. A. Mirkin, *Proc. Natl. Acad. Sci. U. S. A.*, 2016, **113**, 1–6.
- 39 B. S. John and F. A. Escobedo, *J. Phys. Chem. B*, 2005, **109**, 23008–23015.
- 40 U. Agarwal and F. A. Escobedo, *Nat. Mater.*, 2011, **10**, 230–235.
- 41 P. F. Damasceno, M. Engel and S. C. Glotzer, *Science*, 2012, **337**, 453–457.
- 42 F. Smallenburg, L. Filion, M. Marechal and M. Dijkstra, *Proc. Natl. Acad. Sci. U. S. A.*, 2012, **109**, 17886–17890.
- 43 J. Henzie, M. Grünwald, A. Widmer-Cooper, P. L. Geissler and P. Yang, *Nat. Mater.*, 2011, **11**, 131–137.
- 44 H. Lin, S. Lee, L. Sun, M. Spellings, M. Engel, S. C. Glotzer and C. A. Mirkin, *Science*, 2017, **355**, 931–935.
- 45 J. T. McGinley, I. Jenkins, T. Sinno and J. C. Crocker, *Soft Matter*, 2013, **9**, 9119–9128.
- 46 C. L. Phillips and E. Jankowski, *Phys. Rev. E: Stat., Nonlinear, Soft Matter Phys.*, 2012, **86**, 041124.
- 47 C. L. Phillips, E. Jankowski, B. J. Krishnatreya, K. V. Edmond, S. Sacanna, D. G. Grier, D. J. Pine and S. C. Glotzer, *Soft Matter*, 2014, **10**, 7468–7479.
- 48 D. C. Rapaport, *Phys. Rev. E: Stat., Nonlinear, Soft Matter Phys.*, 2004, **70**, 051905.
- 49 D. C. Rapaport, *Phys. Rev. E: Stat., Nonlinear, Soft Matter Phys.*, 2012, **86**, 051917.
- 50 M. A. Horsch, Z. Zhang and S. C. Glotzer, *Soft Matter*, 2010, **6**, 945–954.
- 51 T. D. Nguyen, E. Jankowski and S. C. Glotzer, *ACS Nano*, 2011, **5**, 8892–8903.
- 52 T. D. Nguyen, C. L. Phillips, J. A. Anderson and S. C. Glotzer, *Comput. Phys. Commun.*, 2011, **182**, 2307–2313.
- 53 R. L. Marson, T. D. Nguyen and S. C. Glotzer, *MRS Commun.*, 2015, **5**, 397–406.
- 54 D. Chandler, J. D. Weeks and H. C. Andersen, *Science*, 1983, **220**, 787–794.
- 55 G. Grest and K. Kremer, *Phys. Rev. A: At., Mol., Opt. Phys.*, 1986, **33**, 3628.
- 56 J. A. Anderson, C. D. Lorenz and A. Travesset, *J. Comput. Phys.*, 2008, **227**, 5342–5359.
- 57 D. Frenkel, B. Smit, J. Tobochnik, S. R. McKay and W. Christian, *Comput. Phys.*, 1997, **11**, 351–354.
- 58 P. J. Steinhardt, D. R. Nelson and M. Ronchetti, *Phys. Rev. B: Condens. Matter Mater. Phys.*, 1983, **28**, 784.
- 59 A. Haji-Akbari, M. Engel, A. S. Keys, X. Zheng, R. G. Petschek, P. Palfy-Muhoray and S. C. Glotzer, *Nature*, 2009, **462**, 773–777.
- 60 E. R. Chan, X. Zhang, C. Y. Lee, M. Neurock and S. C. Glotzer, *Macromolecules*, 2005, **38**, 6168–6180.
- 61 M. Kowalik and K. V. Tretiakov, *Comput. Methods Sci. Technol.*, 2010, **16**, 141–146.
- 62 P. F. Damasceno, M. Engel and S. C. Glotzer, *ACS Nano*, 2012, **6**, 609–614.
- 63 K. L. Young, M. L. Personick, M. Engel, P. F. Damasceno, S. N. Barnaby, R. Bleher, T. Li, S. C. Glotzer, B. Lee and C. A. Mirkin, *Angew. Chem., Int. Ed.*, 2013, **52**, 13980–13984.
- 64 P. Biancaniello, A. Kim and J. Crocker, *Phys. Rev. Lett.*, 2005, **94**, 94–97.